Article

Ultrafast Surface Plasmon Resonance Imaging Sensor via the High-Precision Four-Parameter-Based Spectral Curve Readjusting Method

Xueliang Wang,[||] Youjun Zeng,[||] Jie Zhou, Jiajie Chen,* Ruibiao Miyan, Han Zhang, Junle Qu, Ho-Pui Ho, Bruce Zhi Gao, and Yonghong Shao*

Read Online

ACCESS | Metrics & More | Article Recommendations

ABSTRACT: A variety of surface plasmon resonance (SPR) sensing devices have been extensively used in biochemical detection for their characteristics of label-free, highly sensitive, and faster detecting. Among them, the spectrum-based SPR sensing devices have offered us great advantages in high-throughput sensing due to their large dynamic range and the possibility of detection resolution similar to that offered by angle interrogation. This paper demonstrates a spectrum-based SPR imaging sensing system with fast wavelength scanning capability achieved by an acousto-optic tunable filter (AOTF) and a low-cost and speckle-free halogen lamp implemented as the SPR excitation source. Especially, we developed a novel four-parameter-based spectral curve readjusting (4-PSCR) method for data processing, which offered us a faster and more accurate spectral data curve fitting process than the traditional polynomial fitting method. With the configuration, we have also conducted an SPR high-throughput detection of the novel coronavirus (COVID-19) spike protein, proving its application possibility in the screening of COVID-19 with high accuracy. We believe that the higher sensitivity and accuracy of the system have made it readily used in biochemical imaging and detecting applications.
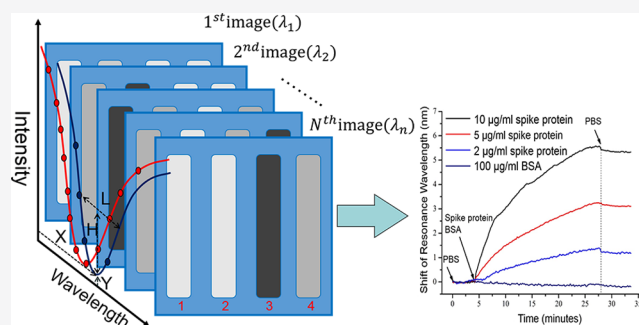
1. INTRODUCTION

Surface plasmon resonance (SPR) sensors are quite suitable for studying nanoscale biochemical reactions because of their unique properties.[1−3] In recent years, the development of imaging-type SPR sensing has greatly increased the detection throughput,[4−7] especially for large-scale antigen−antibody binding detection and imaging.[8] In addition, among the four SPR sensing interrogation modes of intensity, angle, wavelength, and phase, the wavelength interrogation mode is more suitable for SPR imaging for its ability to freely select the optimal excitation light wavelength as well as its large dynamic detection range.[8−11] A typical wavelength interrogation SPR (λSPR) imaging system mainly includes two parts: (i) an optical hardware system for spectral signal recording and (ii) a data processing scheme for resonance wavelength identification.

For the optical hardware part, in a traditional wavelength interrogation SPR sensing system, a broadband light source is commonly utilized as the light source and a spectrometer or optical grating is normally adopted for wavelength analysis. To obtain the information of all different sensing sites on the sensing surface, point or line scanning is needed, which takes more time and introduces additional mechanical noise.[12−14] To realize the fast high-throughput measurement, a novel wavelength-scanning-based SPR sensor is developed.[15] This wavelength scanning method can directly produce the SPR image of the sensing surface without the requirement of mechanical scanning. Compared with the traditional spectrometer or optical-grating-based SPR imaging sensors, the imaging speed and stability of the wavelength scanning SPR sensors can be greatly improved. In the previous studies, our group has developed a series of SPR biosensing systems with high throughput and fast imaging speed. In our early design, a halogen lamp was implemented as the SPR excitation light source, a liquid crystal tunable filter (LCTF) was utilized as the wavelength scanning device, and a CMOS camera was applied as the imaging detector. During the test, the LCTF and CMOS operated in a synchronous way. When a scan cycle was completed, a series of images of the whole sensing surface can be obtained. Subsequently, by analyzing those images, the SPR spectrum in each pixel can be reconstructed.
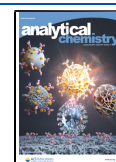
For the data processing part, the spectral data recorded using a spectrometer or grating-CMOS in traditional wavelength interrogation SPR sensors are usually the whole SPR spectrum profile with high spectrum resolution. The resonance wavelength can be identified rapidly by the polynomial fitting method or the spectrum curve centroid calculation method.[16,17] However, for wavelength-scanning-based SPR sensing technologies, the SPR imaging speed is inversely proportional to the number of wavelength sampling points. The more the wavelength sampling points, the slower the SPR imaging speed. Moreover, the sparse sampling of wavelength in SPR curves can lead to inaccuracy when conducting the traditional polynomial fitting methods for resonance wavelength identification. To realize the accurate identification under the sparse sampling mode, a five-parameter polynomial algorithm that only five-wavelength data are recorded in each scanning cycle is proposed.[18] It performs well when the difference between the resonance wavelengths of all sensing sites on the sensing surface is within a few nanometers. Recently, we have also developed an SPR sensor based on fast wavelength scanning and SPR dip tracking combined with a feedback algorithm. It utilizes the densely sampled wavelength data near the resonance wavelength to implement polynomial fitting of the partial SPR curve, and the detection speed is further increased.[19,20] However, if one conducts whole scanning range curve fitting, low-order polynomial fitting cannot accurately retrieve the resonance wavelength position, while high-order polynomial fitting is often greatly affected by the noise near the resonance wavelength, which greatly reduce the sensitivity of the system. Therefore, although one can reduce the wavelength sampling points or conduct partial spectral curve fitting to obtain a higher imaging speed, the wavelength data, especially in the vicinity of the resonance wavelength, becomes scarce and weak, thus leading to inaccuracy of the resonance wavelength results when conducting partial spectral polynomial fitting near the SPR dip.

In this paper, we demonstrate a novel λSPR imaging system. In the hardware part, we employ the AOTF for wavelength scanning so as to improve the detect speed and sensitivity and the halogen lamp is used as the excitation light source to avoid the speckle noise caused by the coherent light source. In the data processing part, a four-parameter-based spectral curve readjusting (4-PSCR) method with high accuracy and noise suppression is developed. It first operates by implementing high-order polynomial curve fitting to get the initial SPR spectral curve in the first scanning period. Then it obtains the following high-precision SPR spectral curves by readjusting the initial curve via four adjustment parameters. This method has shown significant advantages over traditional polynomial fitting methods in terms of noise suppression and SPR peak identification accuracy. Moreover, the detection speed has increased to 0.2 s, which is currently the fastest speed achieved for the λSPR imaging system based on the incoherent light source.[14,21] In addition, considering the background of a worldwide pandemic of Cs-19 nowadays, we also conducted COVID-19 spike protein detection using our system. The feasibility of the system for high-throughput biomolecular detection is verified.

2. EXPERIMENT

2.1. Setup. As shown in Figure 1, the white light from the halogen lamp (GCI-060101, Daheng Optics, Beijing, China) is collimated by a short focal length lens L1 (focus length, FL: 60
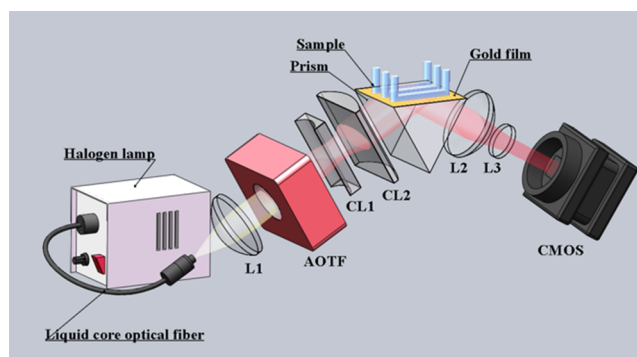

Figure 1. Optical setup of the fast wavelength interrogation SPR imaging system, L1-L3, lens; CL1-CL2, cylindrical lens.

mm). After the modulation of the AOTF (AOTFnC-VIS-TN, AA Opto-electronic, Orsay, France), the white light becomes narrow-band p-polarized light (1.2−4 nm FWHM), and then it is expanded by the cylindrical lens group CL1 (FL: −20 mm) and CL2 (FL: 60 mm) in one direction to form an elliptical beam so as to compensate the distortion of the homemade coupling prism. The incident angle θ on the gold film (50 nm) is about 72.5°. On the top of the gold film, a multichannel PDMS flow cell is mounted, and the reflected light with the information of the sample is imaged by the relay optics of lens L2 (FL: 110 mm) and L3 (FL: 33 mm) to the CMOS (DMK37AUX287, Imaging Source, Bremen, Germany) sensing surface. When conducting the measurement, the AOTF and CMOS are controlled synchronously. After the AOTF switches a primary wavelength, the CMOS carries out multiple exposures to obtain the average intensity map of the sensing surface under that wavelength. When the AOTF finishes a whole spectral period scanning, a series of sensing surface intensity images are obtained. The intensity variation with respect to the scanning wavelengths forms an SPR spectral curve for each pixel, so a series of SPR spectral curves of the two-dimensional sensing surface can be obtained. The resonance wavelength of each detecting point can be calculated by our 4-PSCR algorithm, which will be discussed later. Eventually, a two-dimensional SPR wavelength image of the whole sensing surface is acquired.

2.2. 4-PSCR Algorithm. In order to precisely identify the resonance wavelength, first, we scan the excitation light in the light source's spectrum range of 550 to 750 nm with a shorter wavelength step size of 0.5 nm so that the densely sampled spectrum data $I_{save}[(\lambda_j, I_j)]$ in a wide scanning range is obtained, where (λ_j, I_j) represents the light intensity I_j at the certain wavelength $(j = 0,1,2,3\cdots, j_{max})$. Then, based on $I_{save}[(\lambda_j, I_j)]$, we produce 17th-order generalized polynomial fitting via the least-squares method.

$$f_{save}(\lambda_j) = \sum_{k=0}^{17} a_k \lambda_j^k \tag{1}$$

To better monitor the change of resonance wavelength with a precision level similar to that of the 17th-order polynomial fitting while maintaining faster speed, we define a storage function of $F_{fit}[\lambda_j]$ in a deformed form of f_{save} via four linear transformation parameters

$$F_{fit}[\lambda_j] = H(f_{save}(L(\lambda_j + X))) + Y \tag{2}$$

in which we set a predefined transform matrix D = [H, L, X, Y]^T with the initial value of D_0=[1,1,0,0]^T, where L, H are the transverse, longitudinal stretching coefficients and X, Y are the transverse, longitudinal translation coefficients. After the above storage function is defined, we take the measurement in the resonance region of 600−700 nm. If the sample changes, we will get a new spectrum $I_{detect}[(\lambda_j, I'_j)]$, where I'_j is the new intensity at λ_j, and the initial D_0 is changed. Then, instead of conducting the 17th-order curve fitting, based on eq 2, we adopt the Levenberg−Marquardt method to solve the transform matrix D and obtain the updated fitting curve $F_{fit}(\lambda_j, D)$ as well as its resonance wavelength.[22,23]

The deviation of a measurement value I'_j from its fitting value is expressed by

$$P(D, \lambda_j) = I'_j - F_{fit}(\lambda_j, D) \tag{3}$$

and the sum of squared errors is written as

$$S(D) = \sum_{j=0}^{max} (P(D, \lambda_j))^2 \tag{4}$$

Therefore, in the following steps, our target is to find an optimized transform matrix D via the optimized iterative process so that S(D) and P(D, λ_j) can be infinitely small, and the steps are elaborated below:

Step 1: Initial values of $D_0 = [1,1,0,0]^T$, $\mu = 10$, and $\varepsilon = 10^{-8}$ are set, in which μ is the damping factor to adjust the iteration and ε is the iterative threshold.

Step 2: According to the Levenberg−Marquardt method, we define

$$D_{n+1} = D_n - [J^T J + \mu E]^{-1} J^T F(D_n) \tag{5}$$

where E is the unit matrix and J is the Jacob determinant of F(D, λ_j) expressed by

$$J = \left[\frac{\partial F}{\partial H}, \frac{\partial F}{\partial L}, \frac{\partial F}{\partial X}, \frac{\partial F}{\partial Y} \right] \tag{6}$$

Step 3: Finding the ultimate value D for the resonance wavelength calculation

If $S(D_n) < \varepsilon$ or the number of iterations reaches a certain value, i.e., 200, the iteration is terminated and value D_n is returned.

If $S(D_{n+1}) \geq S(D_n)$, we set the damping factor to $10 \times \mu$ and return to Step 2.

If $S(D_{n+1}) < S(D_n)$, we set the damping factor to $0.4 \times \mu$ and return to Step 2.

Step 4: Obtaining the resonance wavelength λ_{detect}

After the iteration is terminated, the ultimate transform matrix D is obtained. To get an accurate resonance wavelength λ_{detect}, we employ the three spline interpolation on $F_{fit}[\lambda_j]$ under natural boundary conditions,[24] and then we can obtain the resonance wavelength λ_{detect} at the position where $F_{fit}[\lambda_j]$ reaches its minimum value.

Note that identical calculation is conducted in every pixel site so that a two-dimensional resonance wavelength gray value image can be constructed. The algorithm only needs to use several data points to extract the resonance wavelength while retaining a high-precision level similar to high-order polynomial fitting. Theoretically, it needs four data points to get the results because of the four unknown variables; here, we choose 10 data points to further suppress the noise level and meet the dynamic detection range requirement.

To visualize this process, Figure 2 shows an example based on simulation data, in which F_{save} is the initial fitting curve of
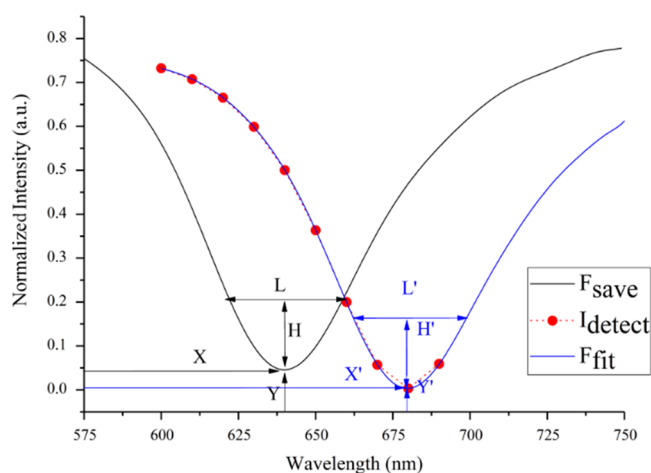

Figure 2. 4-PSCR data processing. Transverse stretching: L to L '; transverse translation: X to X'; longitudinal stretching: H to H '; longitudinal translation: Y to Y'.

the densely sampling SPR spectral profile in a wide spectrum range when the refractive index is $n = 1.33$, while I_{detect} is sparse sampling spectral data points in the range of 600−700 nm when the refractive index of the sample is $n = 1.35$. Through the translation and stretching of four parameters of F_{save} with H', L', X', and Y', the fitting curve F_{fit} can be obtained while retaining the same precision level of high-order polynomial fitting.

We also analyzed the performances of different fitting methods in simulation. The diagonal plane of the prism (BK7, $n = 1.515$ RIU) is coated with a 50 nm gold film, the incident angle of p-light is 75°, the refractive index of the sample is 1.333−1.360 RIU (step size 0.001 RIU), and the spectral range is from 590 to 690 nm. The errors between the theoretical value and fitting value of resonance wavelengths were calculated by different fitting methods (include 2/4/6/8-order polynomial fitting and 4-PSCR method). As the results in Figure 3a indicate, the higher the fitting order, the smaller the error value, the larger the noise, and the 4-PSCR method possesses a similar error value curve to the 8-order polynomial fitting. We further simulated the influence of the signal noise on the resonance wavelength. The signal with noise is generated by the superposition of a uniform random white noise (<0.01 a.u.) on each theoretical SPR curve. Then the root mean square noise values of 8-, 6-order polynomial fitting and 4-PSCR method are 0.16, 0.105, and 0.05 a.u., respectively. As Figure 3b indicates, the 4-PSCR method shows good noise suppression ability over the other two high-order polynomial fitting methods. Therefore, the 4-PSCR method has good calculation accuracy alike the high-order polynomial fitting while maintaining a prominent antinoise ability. In addition, note that the AOTF can generate 2−4 nm FWHM when doing rapid switching of the input wavelengths. To assess the additional error it may introduce compared with the ideal value, we did the corresponding simulations by considering the FWHM in AOTF wavelength switching. The results indicate that a refractive index variation of 0.020 RIU gives a resonance wavelength shifting of 42 nm, while the cumulative resonance wavelength deviation from the ideal
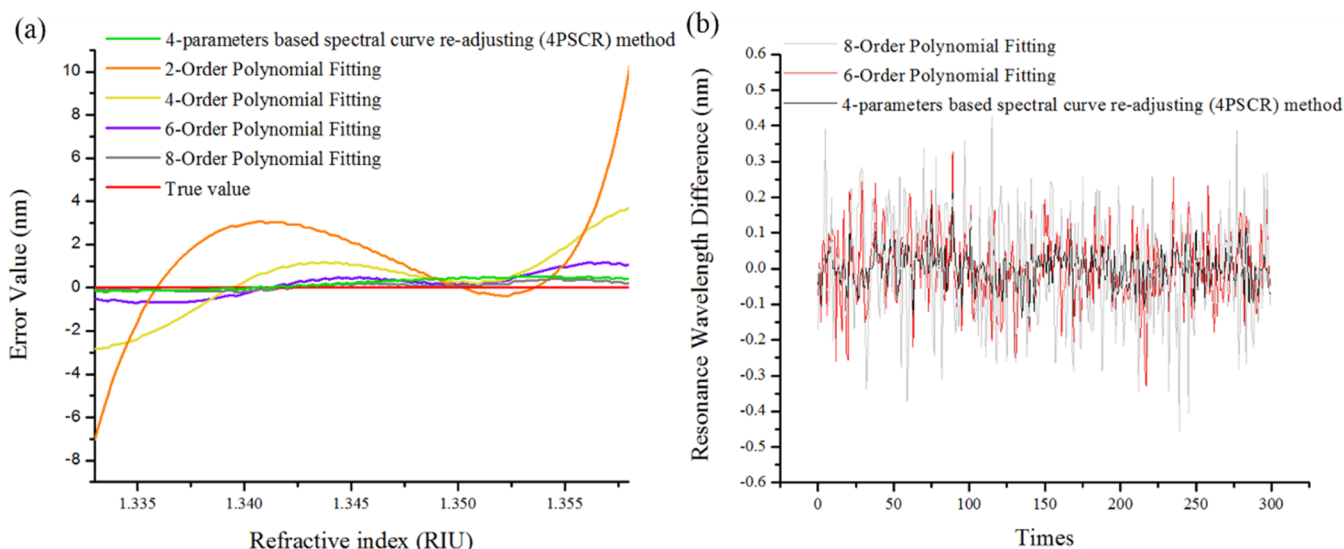
Figure 3. Error comparison among different fitting methods. (a) The error value of the calculated resonance wavelength using different fitting methods. (b) The resonance wavelength noise from 4-PSCR and 6-, 8-order polynomial fitting.

value calculated by the 4-PSCR method is less than 1 nm. There only exists 2.3% (1 nm/42 nm) of uncertainty induced by the AOTF bandwidth, and it is identical to the system noise level. Therefore, it can be neglected and will not affect the resonance wavelength measurement.

3. RESULTS AND DISCUSSION

As shown in Figure 4, fast resonance wavelength interrogation capability based on the 4-PSCR method is experimentally
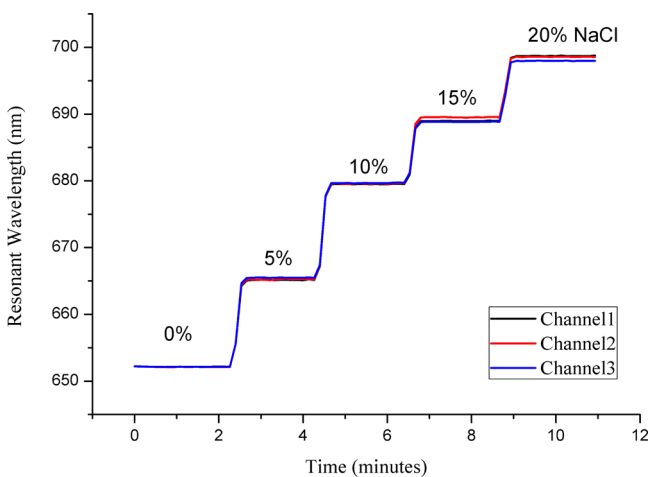

Figure 4. Shift of resonance wavelength versus salt concentration in water (v/v).

demonstrated by detecting the change of refractive index of different salt-water mixtures. The NaCl solution with volume concentrations ranging from 0 to 20% (corresponding to a refractive index ranging from 1.3330 to 1.3700 RIU) is successively injected into the three channels. The time to obtain one λSPR image frame is 200 ms. The measured dynamic detection range of the system is $R = 0.037$ RIU. The variations of three curves are basically the same, which verified the consistency of the system. In addition, based on the equation

$$\sigma_{RI} = \frac{\sigma_n}{\sigma_s}\sigma_{SD} \tag{7}$$

in which σ_s, σ_n are the variation of signal and refractive index, respectively, and σ_{SD} is the root mean square of noise. Therefore, the calculated system resolution σ_{RI} is 1.17×10^{-6} RIU.

We also conducted the real-time monitoring of a near-field ion diffusion process in solution. Two droplets of NaCl solution with concentrations of 0 (left) and 20% (right) were coalesced at the beginning of the test. As shown in Figure 5, a series of resonance wavelength images in time sequence were obtained, and one can clearly see the ion diffusion process in the near-field range of the sensing surface.
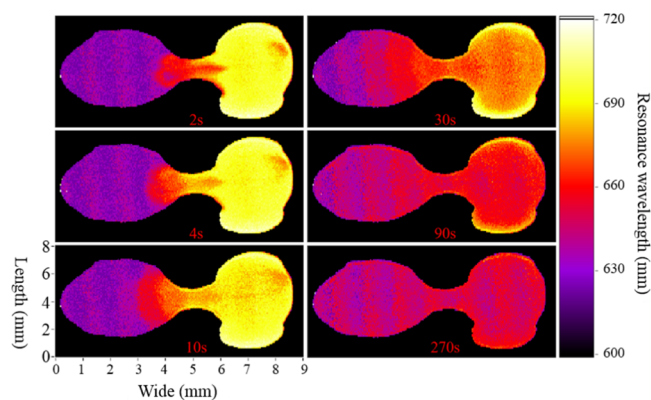

Figure 5. Dynamic monitoring of the near-field ion diffusion process via the false color image of λSPR.

From the beginning of 2020, as the novel coronavirus disease (COVID-19) is spreading globally, reliable laboratory detection of the virus is of crucial importance for early diagnosis and vaccine development. To provide a novel label-free high-throughput detection technology for COVID-19, we conducted experiments that detect the spike protein of COVID-19 using our system. The spike protein was detected by the fabrication of an SPR immune-sensor. First, the chip was incubated in 10 mM 11-mercaptoundecanoic acid (MUA)
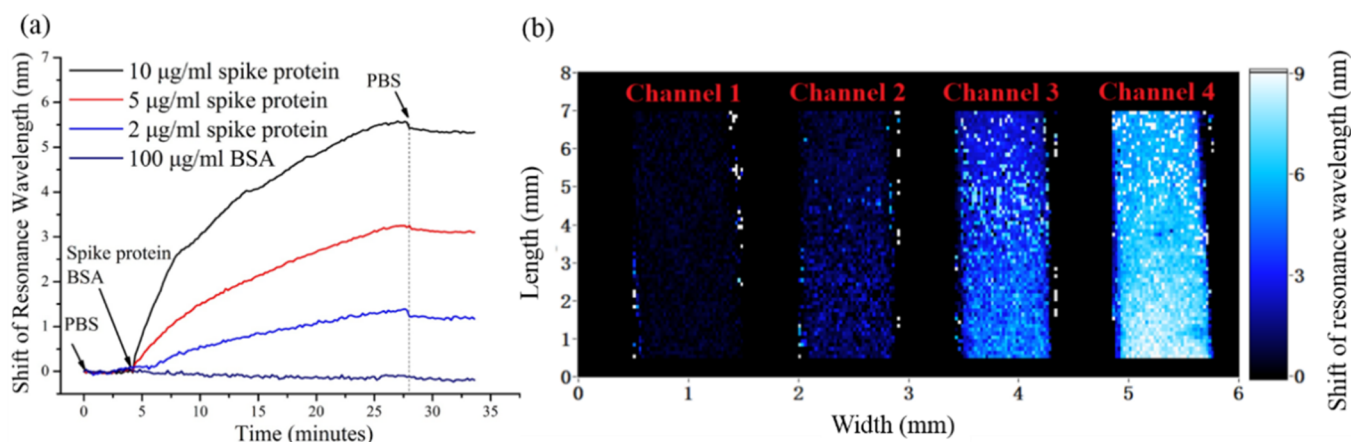
Figure 6. (a) Shift of resonance wavelength at different spike protein concentrations during the experiment. (b) Microfluidic channel λSPR images of 100 μg/mL BSA and 2.0, 5.0, and 10 μg/mL spike protein solution from Channel 1 to Channel 4, respectively.

for 24 h to form a self-assembled monolayer (SAM) on the gold film. After that, we used ethanol and DI water to clean the gold film surface and dried it with nitrogen blowing. Finally, we placed the modified gold film on the prism via matching oil and mounted the multichannel flow cells onto the gold film for subsequent experiments. PBS was injected into each channel to get the baseline. Activation of the carboxyl groups by converting them to N-ester groups was achieved by flow cell infusion of 0.4 mol/L 1-(3-dimethylaminopropyl)-3-ethyl-carbodiimide hydrochloride (EDC) and 0.1 mol/L N-hydroxysuccinimide (NHS) in 0.1 mol/L 2-(N-morpholino)-ethanesulfonic acid sodium salt (MES, pH = 5.5). Then the antibody to the COVID-19 spike protein (S1 subunit) (10 μg/mL) in 10 mM acetate (pH = 4.5) was injected into the channels. The residual activated N-ester groups were blocked by injecting 1 M ethanolamine (pH = 9.0). After each step, PBS was injected to flush the channel until the SPR signal was stable. All experiments were conducted at room temperature, and the flow rate of liquid was set to 10 μL/min. For spike protein detection, 2.0, 5.0, and 10 μg/mL spike protein (S1 subunit) were injected into different channels. In the control experiment, 100 μg/mL bovine serum albumin (BSA) was injected into the reference channel. As Figure 6a shows, only the spike proteins can induce significant changes in the resonance wavelength, which verified the specificity of the sensor. In addition, the λSPR imaging system also provides a 2D biochemical interrogation method. As Figure 6b shows, the shift of the resonance dip is proportional to the concentration of spike protein. The binding results of spike protein in different concentrations can be visualized simultaneously via the 2D detection scheme.

To determine the minimum detection concentration of spike protein and analyze the relationship of the resonance wavelength shift with protein concentration, we further detected lower concentrations of protein, 0.1, 0.2, 0.5, and 1 μg/mL, and the entire test results are shown in Figure 7. The circle dots denote the average resonance wavelength shift of the whole channel when the chemical reaction ends at each concentration with respect to the BSA solution, i.e., the difference between the wavelength shift in the spike protein channel and the shift in the BSA channel. Based on the aforementioned data, the solid line shows the calibration plot corresponding to the shift of resonance wavelength with increasing protein concentration (0.2−10 μg/mL) obtained
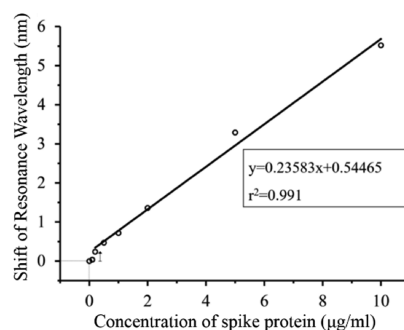

Figure 7. Calibration plot corresponding to the shift of resonance wavelength with increasing spike protein concentration.

from the least-squares fitting method. The linear correlation coefficient (r^2) of the data is 0.991, which exhibits a nearly linear relationship between the shift of resonance wavelength and the protein concentrations ranging from 0.2 to 10 μg/mL. When the concentrations of spike protein decrease to 0.1 μg/mL, there are no measurable changes in the resonance wavelength. Thus, the limit of detection (LOD) of spike protein is estimated to be 0.2 μg/mL. To the best of our knowledge, this is the lowest level that one can achieve using the SPR biosensing scheme for COVID-19 spike protein detection nowadays. Note that although the LOD of this system is still higher than the existing technologies such as ELISA, quick test strip, and field-effect transistor-based biosensor methods, the SPR-based biosensor has its unique advantages of real-time monitoring and high-throughput detection. For example, we can arbitrarily select the regions of interest for detection using our SPRi scheme, which offers great flexibility when doing multisample detections. Moreover, in future development, a much lower LOD can be achieved with the assistance of other technologies, such as nanomaterial-enhanced or optical-assisted signal amplification techniques.

4. CONCLUSIONS

In this paper, we have demonstrated a 4-PSCR-method based wavelength-scanning SPR imaging technique without any mechanical moving parts. A low-cost halogen lamp provides a speckle-free and stable excitation light source, and the AOTF is used as the light source modulation device. Compared to the LCTF, the AOTF is less affected by temperature and can provide better stability, narrower output bandwidth, and faster

switching speed. By incorporating halogen lamp excitation and AOTF scanning with the 4-PSCR algorithm, more accurate SPR wavelength results can be obtained while retaining the same precision level of high-order polynomial fitting. Moreover, it has also greatly reduced the influence of noise near the resonance dip position under the condition of a wide spectrum range, which makes it more suitable for real-time monitoring of 2D biochemical samples. The RI resolution and measured dynamic detection range of our system are 1.17×10^{-6} and 0.037 RIU, respectively, and the SPR imaging speed reaches 0.2 s/frame. In addition, we also applied the λSPRi system for high-throughput detection of COVID-19 spike protein with a detection limit of 0.2 μg/mL. We believe that our proposed spike protein detection scheme can not only provide a solid platform for high-throughput biomolecular detection but also help to improve the medical screening technologies under the outbreak of COVID-19 nowadays.

■ FUNDING

■ AUTHOR INFORMATION

Corresponding Authors

    Jiajie Chen − *College of Physics and Optoelectronics Engineering, Key Laboratory of Optoelectronic Devices and Systems of Ministry of Education and Guangdong Province, Shenzhen University, Shenzhen 518060, China;* ⊙ orcid.org/0000-0002-7200-6626; Email: cjj@szu.edu.cn

    Yonghong Shao − *College of Physics and Optoelectronics Engineering, Key Laboratory of Optoelectronic Devices and Systems of Ministry of Education and Guangdong Province, Shenzhen University, Shenzhen 518060, China;* Email: shaoyh@szu.edu.cn

Authors

    Xueliang Wang − *College of Physics and Optoelectronics Engineering, Key Laboratory of Optoelectronic Devices and Systems of Ministry of Education and Guangdong Province, Shenzhen University, Shenzhen 518060, China*

    Youjun Zeng − *College of Physics and Optoelectronics Engineering, Key Laboratory of Optoelectronic Devices and Systems of Ministry of Education and Guangdong Province, Shenzhen University, Shenzhen 518060, China*

    Jie Zhou − *College of Physics and Optoelectronics Engineering, Key Laboratory of Optoelectronic Devices and Systems of Ministry of Education and Guangdong Province, Shenzhen University, Shenzhen 518060, China*

    Ruibiao Miyan − *College of Physics and Optoelectronics Engineering, Key Laboratory of Optoelectronic Devices and Systems of Ministry of Education and Guangdong Province, Shenzhen University, Shenzhen 518060, China*

    Han Zhang − *College of Physics and Optoelectronics Engineering, Key Laboratory of Optoelectronic Devices and Systems of Ministry of Education and Guangdong Province, Shenzhen University, Shenzhen 518060, China;* ⊙ orcid.org/0000-0002-0166-1973

    Junle Qu − *College of Physics and Optoelectronics Engineering, Key Laboratory of Optoelectronic Devices and Systems of Ministry of Education and Guangdong Province, Shenzhen University, Shenzhen 518060, China*

    Ho-Pui Ho − *Department of Biomedical Engineering, The Chinese University of Hong Kong, Shatin 999077, Hong Kong*

    Bruce Zhi Gao − *Department of Bioengineering and COMSET, Clemson University, Clemson, South Carolina 29634, United States*

Complete contact information is available at:
https://pubs.acs.org/10.1021/acs.analchem.0c03347

Author Contributions

‖X.W. and Y.Z. contributed equal to the article.

Notes

The authors declare no competing financial interest.

■ REFERENCES

(1) Nelson, B. P.; Grimsrud, T. E.; Liles, M. R.; Goodman, R. M.; Corn, R. M. *Anal. Chem.* **2001**, *73*, 1−7.

(2) Homola, J. *Chem. Rev.* **2008**, *108*, 462−493.

(3) Zhou, J.; Zeng, Y.; Wang, X.; Wu, C.; Cai, Z.; Gao, B. Z.; Gu, D.; Shao, Y. *Sens. Actuators, B* **2020**, *304*, 127391.

(4) Zeng, Y.; Zhou, J.; Xiao, X.; Wang, L.; Qu, J.; Li, X.; Gao, B. Z.; Shao, Y. *Plasmonics* **2019**, 1497.

(5) Beusink, J. B.; Lokate, A. M. C.; Besselink, G. A. J.; Pruijn, G. J. M.; Schasfoort, R. B. M. *Biosens. Bioelectron.* **2008**, *23*, 839−844.

(6) Ke, H.; Du, X.; Wang, L.; Wang, X.; Zhu, J.; Gao, Y.; Peng, B.; Hao, H.; Cai, N. *Anal. Methods* **2020**, *12*, 3038.

(7) Wong, C. L.; Olivo, M. *Plasmonics* **2014**, *9*, 809−824.

(8) VanWiggeren, G. D.; Bynum, M. A.; Ertel, J. P.; Jefferson, S.; Robotti, K. M.; Thrush, E. P.; Baney, D. M.; Killeen, K. P. *Sens. Actuators, B* **2007**, *127*, 341−349.

(9) Sereda, A.; Moreau, J.; Canva, M.; Maillart, E. *Biosens. Bioelectron.* **2014**, *54*, 175−180.

(10) Otsuki, S.; Ishikawa, M. *Biosens. Bioelectron.* **2010**, *26*, 202−206.

(11) Ng, S. P.; Wu, C. M. L.; Wu, S. Y.; Ho, H. P. *Opt. Express* **2011**, *19*, 4521−4527.

(12) Yuk, J. S.; Kim, H.-S.; Jung, J.-W.; Jung, S.-H.; Lee, S.-J.; Kim, W. J.; Han, J.-A.; Kim, Y.-M.; Ha, K.-S. *Biosens. Bioelectron.* **2006**, *21*, 1521−1528.

(13) Bolduc, O. R.; Live, L. S.; Masson, J.-F. *Talanta* **2009**, *77*, 1680−1687.

(14) Bardin, F.; Bellemain, A.; Roger, G.; Canva, M. *Biosens. Bioelectron.* **2009**, *24*, 2100−2105.

(15) Jung, J.-W.; Jung, S.-H.; Kim, H.-S.; Yuk, J. S.; Park, J.-B.; Kim, Y.-M.; Han, J.-A.; Kim, P.-H.; Ha, K.-S. *Proteomics* **2006**, 1110.

(16) Owega, S.; Poitras, D. *Sens. Actuators, B* **2007**, *123*, 35−41.

(17) Chinowsky, T. M.; Jung, L. S.; Yee, S. S. *Sens. Actuators, B* **1999**, *54*, 89−97.

(18) Sereda, A.; Moreau, J.; Boulade, M.; Olivéro, A.; Canva, M.; Maillart, E. *Sens. Actuators, B* **2015**, *209*, 208−211.

(19) Zeng, Y.; Wang, L.; Wu, S.-Y.; He, J.; Qu, J.; Li, X.; Ho, H.-P.; Gu, D.; Gao, B. Z.; Shao, Y. *Opt. Express* **2016**, *24*, 28303.

(20) Zeng, Y.; Wang, L.; Wu, S.-Y.; He, J.; Qu, J.; Li, X.; Ho, H.-P.; Gu, D.; Gao, B.; Shao, Y. *Sensors* **2017**, *17*, 90.

(21) Zeng, Y.; Hu, R.; Wang, L.; Gu, D.; He, J.; Wu, S.-Y.; Ho, H.-P.; Li, X.; Qu, J.; Gao, B. Z.; Shao, Y. *Nanophotonics* **2017**, *6*, 1017.

(22) Steinier, J.; Termonia, Y.; Deltour, J. *Anal. Chem.* **1972**, *44*, 1906−1909.

(23) Moré, J. J. The Levenberg-Marquardt algorithm: Implementation and theory. In *Numerical Analysis*; Springer: Berlin, Heidelberg, 1978, *630*, 105, DOI: 10.1007/BFb0067700.

(24) Reinsch, C. H. *Numer. Math.* **1971**, *16*, 451−454.